Biomaterials Advances 164 (2024) 213985

Contents lists available at ScienceDirect

Biomaterials Advances

journal homepage: www.journals.elsevier.com/materials-science-and-engineering-c

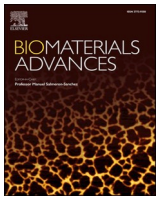

Combining three-dimensionality and CaP glass-PLA composites: Towards an efficient vascularization in bone tissue healing

Celia Ximenes-Carballo [a], Sergi Rey-Viñolas [a], Barbara Blanco-Fernandez [a], Soledad Pérez-Amodio [a,b,c], Elisabeth Engel [a,b,c,**], Oscar Castano [a,b,d,e,*]

[a] Institute for Bioengineering of Catalonia (IBEC), The Barcelona Institute of Science and Technology (BIST), Barcelona, Spain
[b] CIBER en Bioingeniería, Biomateriales y Nanomedicina, CIBER-BBN, Madrid, Spain
[c] IMEM-BRT group, Materials Science and Engineering, Polytechnical University of Catalonia (UPC), Barcelona, Spain
[d] Electronics and Biomedical Engineering, University of Barcelona (UB), Barcelona, Spain
[e] Nanobioengineering and Biomaterials, Institute of Nanoscience and Nanotechnology (IN2UB), Barcelona, Spain

ARTICLE INFO

Keywords:
Bone angiogenesis
3D-printed porosity
Composite
Polylactic acid
Calcium phosphate

ABSTRACT

Bone regeneration often fails due to implants/grafts lacking vascular supply, causing necrotic tissue and poor integration. Microsurgical techniques are used to overcome this issue, allowing the graft to anastomose. These techniques have limitations, including severe patient morbidity and current research focuses on stimulating angiogenesis *in situ* using growth factors, presenting limitations, such as a lack of control and increased costs. Non-biological stimuli are necessary to promote angiogenesis for successful bone constructs. Recent studies have reported that bioactive glass dissolution products, such as calcium-releasing nanoparticles, stimulate hMSCs to promote angiogenesis and new vasculature. Moreover, the effect of 3D microporosity has also been reported to be important for vascularisation *in vivo*. Therefore, we used room-temperature extrusion 3D printing with polylactic acid (PLA) and calcium phosphate (CaP) based glass scaffolds, focusing on geometry and solvent displacement for scaffold recovery. Combining both methods enabled reproducible control of 3D structure, porosity, and surface topography. Scaffolds maintained calcium ion release at physiological levels and supported human mesenchymal stem cell proliferation. Scaffolds stimulated the secretion of vascular endothelial growth factor (VEGF) after 3 days of culture. Subcutaneous implantation *in vivo* indicated good scaffold integration and blood vessel infiltration as early as one week after. PLA-CaP scaffolds showed increased vessel maturation 4 weeks after implantation without vascular regression. Results show PLA/CaP-based glass scaffolds, made *via* controlled 3D printing, support angiogenesis and vessel maturation, promising improved vascularization for bone regeneration.

1. Introduction

Bone tissue can repair itself naturally through a physiological process called bone healing, which includes inflammation, cartilaginous callus formation, endochondral ossification, and remodeling [1]. However, critical bone defects following large trauma, tumor resection, or congenital diseases require external intervention [2,3]. Autografts are the gold standard treatment due to excellent biocompatibility; however, high patient morbidity and limited grafting volume hamper their application. Allografts can also be used to support bone healing, but they present a greater risk of immune rejection and infection [4,5]. On the other side, synthetic materials such as mega prosthesis, collagen/bone morphogenic protein (BMP) sponges, or induced membranes ("Masquelet"), have been used to fill in bone defects. However, these strategies have significant drawbacks and limited regeneration potential. It is therefore necessary to develop new scaffolds for improving bone regeneration [6].

Bone comprises both a non-mineralized organic part (mainly collagen) and a mineralized inorganic part (mainly hydroxyapatite). Research in recent years has focussed on polymeric-based composites doped with ceramics in order to compensate for the fragility inherent in ceramics alone while improving biodegradability and osteoconductive

* Correspondence to: O. Castano, University of Barcelona (UB), Barcelona, Spain.
** Correspondence to: E. Engel, Institute for Bioengineering of Catalonia (IBEC), The Barcelona Institute of Science and Technology (BIST), Barcelona, Spain.
E-mail addresses: eengel@ibecbarcelona.eu (E. Engel), oscar.castano@ub.edu (O. Castano).

https://doi.org/10.1016/j.bioadv.2024.213985
Received 27 February 2024; Received in revised form 30 July 2024; Accepted 2 August 2024
Available online 10 August 2024
2772-9508/© 2024 The Authors. Published by Elsevier B.V. This is an open access article under the CC BY-NC-ND license (http://creativecommons.org/licenses/by-nc-nd/4.0/).

properties [7].

Aside from the chemical composition of the bone itself, porosity has also been considered when designing scaffolds for bone tissue engineering. Macroporosity is one of the most important needed features for 3D scaffolds for a healing process in the form of an interconnected open pore network. Porosity of >60–70 %, and macropore sizes in the diameter range between 100 and 500 μm are essential prerequisites for enabling cell infiltration, nutrient diffusion, and vascularization [8,9]. 3D porous scaffolds increase bone ingrowth because of better deposition of the endogenous cell-extracellular matrix [7,10]. Moreover, 3D porosity is needed to enhance nutrient and oxygen transport, as well as to allow vascularization, cell infiltration, and waste removal [3,10,11]. These aspects converge in the need for an appropriate vasculature to obtain not only healing of the tissue but also efficient regeneration leading to the mitigation or elimination of bone scar.

Additive manufacturing techniques permit the deposition of material in a layer-by-layer manner, allowing complete control of the overall internal and external scaffold structure. For instance, it allows the fabrication of patient-specific scaffolds using computer-aided design (CAD) models based on molecular resonance imaging (MRI) and computed tomography (CT) scans [12]. Moreover, the porosity of the scaffold can be controlled in terms of geometry, size, and interconnectivity, allowing the fabrication of complex scaffolds in a reproducible manner [6,13], and solving problems inherent in other manufacturing techniques [14–19]. Ceramics have been 3D printed with the use of binders [13,20], and further processed at higher temperatures (scaffold sintering) to harden the scaffold and eliminate any organic residues [21]. Fused deposition modeling (FDM) has also been used to deposit both polymer and composite materials in a complex 3D shape [22,23]. Nevertheless, low-temperature extrusion-based 3D printed ceramic scaffolds are mainly fabricated in combination with viscous hydrogels, such as collagen, alginate, and gelatin, which don't have the mechanical stability required for load-bearing bone zones [24].

Therefore, synthetic materials such as polylactic acid (PLA) have been widely used due to their batch-to-batch reproducibility, their biocompatibility, and the ease of adjusting their thermal properties. By combining isomers, PLA degradability can be easily controlled to match that of the tissue of interest. Moreover, it can be processed using a myriad of techniques. However, PLA bioactivity is low. Hence, composites have been investigated for use in bone regeneration. Specifically, the use of calcium phosphate (CaP) based glass scaffolds could improve PLA properties to obtain a material that matches the chemical, mechanical, and biological needs of bone tissue.

Previous works in our group from Oliveira et al. [25,26] showed the fact that embedding a high Ca^{2+}-releasing composition for nanoparticles embedded in a 2D PLA electrospun scaffold dramatically enhanced angiogenesis through controlled calcium release in an angiogenic bioactive extracellular range [27–30] in a bone healing environment. In another study, validation was carried out on a 2D microfluidic model for chemotaxis testing in endothelial cells within a controlled microenvironment, where the same nanoparticles in the fibers stimulated mesenchymal stem cells to express a chemotactic secretome, where, in addition to VEGF, OPN was found an essential chemotactic contributor to blood vessel sprouting [31].

In this study, a 3D printed extrusion-based approach has been used to control macro- and microporosity of composite scaffolds made of PLA and CaP-based glass scaffolds to fabricate an innovative 3D construct with a high calcium-releasing architecture to induce a consistent vascularization. To do this, CaP previously developed [25,26,31–33] was combined with PLA solutions and subsequently 3D printed. The CaP-based glass scaffolds were developed to offer different advantages over other ceramics, such as low-temperature manufacture, physiologically relevant ion release to trigger bone bioactivity, the possibility of ionic doping, a non-diffusion dependent mechanism of release, and better processability. The scaffold's microporosity and geometry were analyzed by field-emission scanning electron microscopy (FE-SEM). Calcium release environment pH and thermal and mechanical properties were also assessed. Cell adhesion, toxicity, proliferation, and vascular endothelial growth factor (VEGF) production were studied using human bone marrow-derived stem cells (hMSCs). Finally, the angiogenic potential of the scaffolds was evaluated using an *ex ovo* chick chorioallantoic membrane (CAM) assay and a subcutaneous *in vivo* mouse model.

2. Materials and methods

2.1. Materials

PLA (70/30 L-Lactide/DL-Lactide copolymer) was purchased from Corbion. Titanium (IV) tetraisopropoxide was obtained from Alfa Aesar. Metallic calcium and metallic sodium, and hexane, were purchased from Panreac. Absolute ethanol and paraformaldehyde (PFA) were acquired from VWR and Electron Microscopy Sciences, respectively. 3D printer tips and cartridges were purchased from Nordson. HyClone™ was obtained from GE Healthcare. L-glutamine, penicillin-streptomycin, αMEM, the Quant-it™ PicoGreen™ dsDNA assay kit, and all the plates for cell culture were purchased from Thermofisher. Human VEGF DuoSet® ELISA kit was purchased from R&D Systems™. The rest of the materials and reagents were purchased from Merck.

2.2. Precursors and reagent preparation

Precursors were prepared in the laboratory as previously reported [34]. Briefly, both metallic calcium and sodium (98 %, and 99.8 % respectively) were refluxed in dry 2-methoxy ethanol. Phosphorous ethoxide was synthesized by refluxing phosphorus pentoxide in absolute ethanol. Titanium precursor was obtained by dissolving titanium (IV) isopropoxide (97 %) dry absolute ethanol. 1,4-dioxane (1,4-Dioxane ReagentPlus®, ≥99 %) was previously distilled with metallic sodium.

2.3. Calcium phosphate nanoparticle synthesis

CaP particles with a composition and percentage molar ratios of 44.5 % P_2O_5: 44.5 % CaO: 6 % NaO: 5 % TiO_2 (named G5) were synthesized as previously reported [25]. Briefly, calcium, sodium, and titanium precursors were mixed in an inert atmosphere and kept in a syringe. Then, 1,4-Dioxane (ratio volume precursor solution *vs* volume 1,4-Dioxane 1:3) was added and subsequently, phosphate precursor was introduced (1 mL/h, 4 °C). Afterward, a solution based on the amount of titanium present (1Ti: 60 H_2O: 0.3 NH_3OH: 12 ethanol) was added (2.5 mL/h, 4 °C). The reaction mixture was then aged at 70 °C for four days. The resulting solution was washed three times with absolute ethanol and once with hexane. G5 nanoparticles were recovered by centrifugation at 20000 rpm, dried, and milled into a fine powder using an agate mortar.

G5 nanoparticles were characterized by X-ray spectroscopy (EDS) analysis using an SEM coupled with an EDS detector (Quanta Q200, FEI Company), and by previous carbon sputtering.

2.4. Acetone scaffold preparation

PLA (70/30 L-Lactide/DL-Lactide copolymer) 14 % *w/v* solutions with and without G5 were prepared in acetone. For scaffolds containing G5, different ratios were dispersed in acetone using an ultrasonic processor (30 % amplitude, 1 s. pulses, 30 s.) (Table 1). PLA and G5 solutions were poured into dispensing systems (3 cc) and printed using a G27 (200 μm diameter) tip at RT.

A 3D-Discovery (RegenHU) direct writing tool was used to print the scaffolds. The volatility of acetone rose during printing, so we carried out a controlled solvent displacement process. After being printed, scaffolds were recovered by *ex situ* solvent displacement using ultrapure water. Scaffolds were also printed under *in situ* continuous solvent displacement (marked with*). To do this, the blend was directly extruded into a well with ultrapure water, enabling acetone

Table 1
Setup parameters to produce the different types of scaffolds. RT: Room Temperature. PSI: pounds-force per square inch.

Material	g5 (%w/w)	Pressure (PSI)	Speed (mm/s)	T°/environment
PLA	0	20–30	7	RT/air
PLAg520	20	20–30	7	RT/air
PLA*	0	20–30	10–15	RT/water
PLAg5*20	20	20–30	10–15	RT/water
PLAg5*50	50	20–30	10–15	RT/water

displacement and removal, and PLA precipitation immediately after being extruded. The parameter settings for each type of scaffold are specified in Table 1.

Scaffolds were freeze-dried, cut with a Harris Uni-Core™ 6 mm punch (Whatman plc), and stored in a desiccator until further use.

2.5. Physicochemical characterization

2.5.1. Scaffold microstructure and morphological evaluation

We took advantage of the shear thinning properties of the slurries to improve the accuracy and stability of the shapes in the 3D printed structures, and to provide a consistent pore structure within the printed scaffolds. To evaluate the scaffold microstructure, scaffolds were coated with a thin layer of carbon and observed using a Nova NanoSEM 230 FEI Ultra-High-Resolution Field Emission Scanning Electron Microscopy (FE-SEM, FEI Company). Strut and pore widths, pore area, pore perimeter, and strut circularity were measured using the Image J software. The printability index (Pr) was evaluated following Eq. (1 [35]

$$P_r = \frac{(pore\ perimeter)^2}{16\ x\ Pore\ area}. \quad (1)$$

2.5.2. Scaffold macroporosity and particle distribution

Scaffold porosity was analyzed using a high-resolution 3D X-ray Microscopy Skyscan1272 (Bruker), at 60 kV, 9 μm/pixel resolution. The step was settled at 0.2 degrees, and an Al 0.25 filter was used. Data were reconstructed using nRecon (v 1.7.3.0, Bruker microCT), images were rendered with CTvox (v 3.2.0.0, Bruker microCT), and porosity was analyzed with CTAn (v 1.16.9.0, Bruker microCT). For the reconstruction, smoothing was settled at 1, and the ring artifact correction at 9. Beam hardening correction was not applied.

Alizarin red staining was performed to visualize the glass incorporation into the scaffolds. Samples were stained with Alizarin Red S (40 mM, pH 4.2) for 10 min, washed with water, and imaged using a Macro Olympus MVx10 (Olympus Corporation).

2.5.3. Scaffold wettability by water contact angle

To determine material wettability, ink solutions were cast onto a glass microscope slide and smoothed with a spatula. Then, acetone was displaced with ultrapure water to obtain films that were freeze-dried, and then 3 μL of ultrapure water was deposited on top of the film before analysis. The water contact angle was assessed using an OCA15 Plus Contact Angle (DataPhysics).

2.5.4. Calcium release

Eight-layer scaffolds were immersed in 4-(2-hydroxyethyl)-1-piperazineethanesulfonic acid (HEPES) (pH 7.2–7.4, 10 mM in ultrapure water; >99.5) at a 50 μL/mg scaffold ratio and incubated at 37 °C in a humid atmosphere. At each time point (1, 3, 7, 14, and 21 days), aliquots were collected and stored at −20 °C until further use. Calcium was detected using the O-cresolphtalein complexone colorimetric method [36,37]. The pH of each sample of the solution was also analyzed using a pH&ION-Meter GLP 22+ (Crison).

2.5.5. Scaffold thermal properties

Polymer crystallinity was determined by differential scanning calorimetry (DSC-Q20, TA Instruments). Samples were submitted to two cycles of cooling-heating from −90 °C to 200 °C at a rate of 10 °C/min. Glass transition temperature (Tg) values were taken from the second heating cycle measuring the small step around 60 °C. Enthalpies from melting and crystalline states were calculated by integrating the peaks of melting and crystallization (Tm and Tc) temperatures obtained on the first cycle, using the TA Universal Analysis 2000 software. The crystallinity of the polymeric fraction was calculated using Eq. 2, where H_m^o is the standard melting enthalpy for 100 % crystalline PLA (93.1 J/g) [38]

$$X_c = \frac{\Delta H_m - \Delta H_c}{\Delta H_m^o}. \quad (2)$$

The effective glass loading on the scaffolds was evaluated by thermogravimetric analysis (TGA Q5000, TA instruments). Samples were heated from RT to 900 °C at a heating rate of 10 °C/min in air. This data was used to recalculate the DSC polymer weight on particle-containing samples.

2.5.6. Mechanical properties

Compression tests were performed using a uniaxial mechanical testing machine (Zwick 0.5 N, Zwick/Roell) with a 200 N loading cell. Samples were tested at 10 % deformation per minute, with a 0.05 N of preloading, until reaching 50 % deformation. Scaffolds were immersed in PBS at RT when performing the assays. For each composition, three cylindric scaffolds (6 mm diameter, 3 mm height) were tested.

2.6. In vitro characterization

2.6.1. Cell culture

Human mesenchymal stem cells (hMSC) from bone marrow [39] were expanded in Alpha minimum essential medium (αMEM) supplemented with 16.5 % of foetal bovine serum HyClone™, 1 % of L-glutamine (200 mM), and 1 % of penicillin-streptomycin (10,000 U/mL). Medium was replaced every 3–4 days. Cells were incubated in a humid atmosphere at 37 °C and 5 % CO_2. Cells up to passage 6 were used.

2.6.2. Cell seeding on scaffolds: Scaffold biocompatibility

Scaffolds were sterilized using UV light, placed in a low attachment 96-well plate (Nunclon), and washed with 30 % ethanol (99.5 %) solution and culture media. Next, wet scaffolds were incubated overnight in culture medium at 37 °C, 5 % CO2, before seeding 40,000 hMSCs on each scaffold.

hMSCs were cultured on scaffolds for 1 day and fixed with 4 % paraformaldehyde for 10 min. Cells were permeabilized using a Triton PBS-gly 0.1 % solution for 5 min. Actin filaments were stained using phalloidin red (100 nM, RT) and cell nucleus using 4′,6-diamidino-2-fenilindol (DAPI) (100 nM, 1 min, RT, Abcam). After washing, scaffolds were observed using an inverted microscope (DM IL LED microscope, Leica Microsystems).

2.6.3. Scaffold-conditioned media

Scaffolds (20 mg/mL) were sterilized and incubated in culture media for 5 days. Culture medium was changed every day. For each day, aliquots were collected and stored at −80 °C or added to cells for stimulation. These media will be referred to as conditioned media.

2.6.4. Scaffold cytocompatibility

Scaffold cytocompatibility was evaluated by quantifying the lactate dehydrogenase (LDH) release. Cells were seeded onto 96 well plates (10,000 per well) and left to attach overnight. Then, conditioned media from 24 and 48 h were added separately to cells for 24 h. Cell' SN was recovered and evaluated for LDH release (Cytotoxicity Detection Kit PLUS (LDH), Roche), following the manufacturer's instructions.

Absorbance was read at 492 nm with a reference wavelength of 610 nm using a Benchmark Plus Microplate Reader (Bio-Rad).

2.6.5. Cell proliferation and VEGF production

Cells were seeded onto 48-well plates (6000 hMSCs per well) and cultured in the presence of conditioned media for 1, 3, and 5 days. Conditioned media were refreshed every day. Cell proliferation was quantified by determining the dsDNA. Cells were washed with PBS and lysed with 1× TE buffer. Then, dsDNA was determined using the Quant-it™ PicoGreen™ dsDNA assay kit, following the manufacturer's instructions.

For VEGF production, supernatants were collected and stored at −80 °C at each time point. VEGF was then quantified using the Human VEGF DuoSet® ELISA kit, following the manufacturer's instructions. VEGF concentrations were normalized by their corresponding dsDNA amount.

2.6.6. Alizarin red staining

Cells were seeded onto 48-well plates (6000 hMSCs per well) and cultured in the presence of conditioned media. Conditioned media were refreshed every day. After 5 days, cells were fixed with 4 % paraformaldehyde and stained with Alizarin Red S (40 mM, pH 4.2) for 20 min. Images were taken with an inverted microscope (DM IL LED microscope, Leica Microsystems). Positive control for mineralization was also performed. Briefly, hMSCs were stimulated with bone differentiation media (complete culture media supplemented with 1 nM dexamethasone, 10 mM beta-glycerolphosphate, and 50 μM L-Ascorbic acid, according to the cell provider's instructions).

2.7. In vivo subcutaneous model for biocompatibility and angiogenic evaluation

All animal procedures were approved by the Animal Experimentation Committee (CEA) of the Government of Catalonia (project number 10728). Scaffolds were implanted in sixteen eight-week-old male CD1 mice (Charles River Laboratory). Scaffolds of 6 mm in diameter were sterilized for 30 min with UV (15 min per each side) and soaked in physiological serum before implantation. Subcutaneous pockets were made on the backs of the mice, by making a 1 cm incision, into which the scaffold was inserted. Four scaffolds were implanted in each mouse. Of these four scaffolds, two were PLA* and two contained G5. A total of eight animals per condition were used (Fig. 8. A). Pockets were closed by performing four simple stitches (Silk, 4/0 stitches, Aragó lab).

After 1 and 4 weeks, four animals from each group were sacrificed by cervical dislocation. Scaffolds and surrounding tissue were harvested and fixed in 10 % formalin solution for 24 h. Then, specimens were paraffin-embedded, and sections (5 μm) were stained using H&E, CD31, and αSMA. Immunostaining and histological studies were performed at the Histopathology Core Facility of the IRB (Barcelona).

A blinded semiquantitative study of the inflammatory reaction was made. Briefly, a score of from 0 (none) to 5 (very intense) was assigned by an expert pathologist to evaluate the inflammatory infiltration surrounding the material. The number of multinucleated giant cells, the degree of fibrosis, and the presence of microhemorrhage were studied. Then, the sum of all the scores for each sample (up to 20) was used to assign a new interval for assessing the overall inflammatory response.

Angiogenesis was evaluated by quantifying CD31+ vessels with a lumen found inside the scaffold area using the NDP.view2 software (Hamamatsu). The vessel number was normalized by the total area considered. Furthermore, the same software was used to measure vessel wall thickness on αSMA+ vessels. Two measurements per vessel wall were performed.

2.8. Statistics

Results are represented as mean ± standard deviation. One or two-way ANOVA was used to assess statistical differences between the groups, with a *post-hoc* Tukey's test using GraphPad Prism 9.2. (San Diego, CA, US). Results with a *p*-value below 0.05 ($p < 0.05$) were considered statistically significant.

3. Results

3.1. Scaffold macrostructure and printability

Scaffolds with the described architecture were printed successfully (Fig. 1). The pore was designed to be a square of 1 mm per side (1 mm^2). Scaffolds showed printability indexes around 1, resulting in high geometric accuracy (Fig. 1B). Our results indicate that pore width comes closer to the theoretical value when the percentage of particles is increased (Table 2). Moreover, the scaffold measured from the top view showed strut values close to the theoretical (200 μm). However, strut circularity evaluated from the scaffold's cross-section showed values around 0.5, indicating that the scaffold's strut was flatter than expected (Table 2).

3.2. Scaffold microstructure

The scaffold microstructure was evaluated by FE-SEM. The scaffold surface features were dependent on the moment at which the solvent was displaced (Fig. 2). FE-SEM images indicate that smooth surfaces resulted from displacing the solvent after deposition of the whole structure, whereas the presence of pores is observed when a rapid and constant solvent displacement was performed during the extrusion process (Fig. 2A). Pores on G5 containing scaffolds look smaller than PLA*(Fig. 2A).

Rapid precipitation of the PLA induced a core-shell morphology, with a gradient of pore size ranging between larger voids on the surface and small pores in the strut center (Fig. 2B). In addition, PLA precipitated after printing had a more uniform strut, with no internal or external porosity at all. G5-containing scaffolds showed a homogeneous cross-section (Fig. 2B).

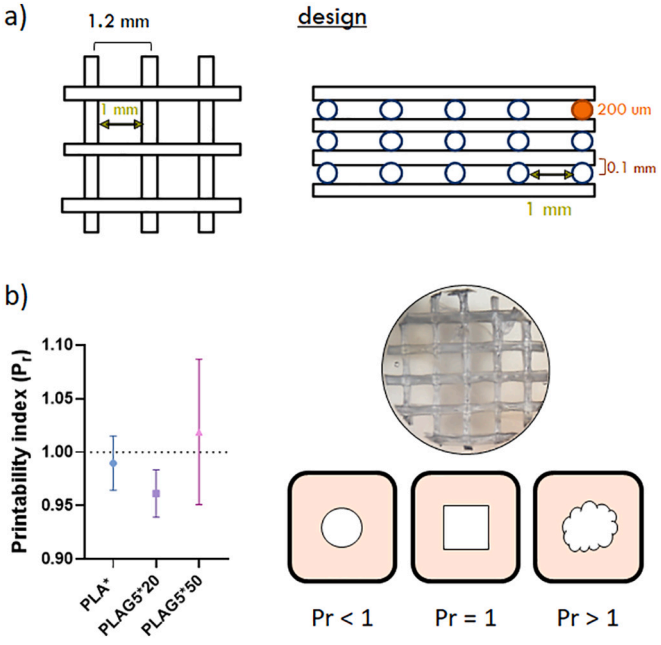

Fig. 1. Scaffold design and shape fidelity. (a) Scaffold design planned to be printed with a 200 μm tip. (b) Printability index (Pr) of the different scaffolds. On the right, image of the printed scaffold (top) and interpretation of the Pr: Pr values =1 define high shape fidelity, whereas Pr values over and under 1 define closed or irregular pores [35].

Table 2
Nominal values determined by ImageJ analysis of FE-SEM images. Statistical differences with PLA* scaffolds are indicated with an asterisk (*). Statistical differences with the theoretical parameters are indicated with Δ.

	Strut (μm)	Strut circularity	Pore (μm)
PLA*	249.00 ± 44.00	0.55 ± 0.07	801.16 ± 92.84 Δ
PLAG5*20 %	189.00 ± 44.00*	0.50 ± 0.00	886.65 ± 34.67*
PLAG5*50 %	210.43 ± 26.99	0.60 ± 0.07	974.43 ± 68.12*

3.3. Scaffold microporosity, wettability, and particle distribution

Both μCT and FE-SEM analysis indicate that scaffolds had a fully interconnected macropore structure (Fig. 3A - B). Scaffold porosities ranged between 85 and 92 %, with pure PLA* scaffolds being slightly more porous than G5-containing ones (Fig. 3C). Due to the resolution limitations of the equipment, only G5 aggregates were noted. Despite this, the presence of the particles was detected throughout all the structures, suggesting a homogeneous distribution of the G5 on the polymeric matrix (Fig. 3D). This observation was confirmed by staining scaffolds with Alizarin red, showing higher intensity when the G5 percentage was increased (Fig. 3E).

3.4. Calcium release

Results showed that the higher the particle content, the greater the amount of calcium released, achieving a maximal release of around 12.51 mM for PLAG5*50 scaffolds at 21 days (Fig. 4A). Calcium release is expected to be higher at longer time points since scaffold degradation gradually exposes the G5 embedded within scaffold-printed struts. Indeed, as the scaffolds further degrade, more of the G5 is accessible and exposed for ion release, which increases with time. Moreover, scaffold microporosity may also affect calcium release. This can be evidenced by the increase in calcium release (from 2.27 to 8.07 mM) found when the solvent is displaced from the beginning of the printing process (*in situ*) (Fig. 4A, PLAG520 *vs.* PLAG5*20). pH was similar in all scaffolds tested (Fig. 4B).

3.5. Scaffold thermal and mechanical properties

Scaffold thermal properties were evaluated by DSC. All the scaffolds showed an amorphous behavior, with T_g values around 60 °C (Table 3). The addition of G5 did not affect the T_g. Scaffolds showed less G5 percentage than the theoretical value, which was more pronounced at higher G5 content.

Scaffolds showed a proximate compressive elastic modulus in the range of 6–9 MPa (Table 3), which was not affected by the addition of G5.

3.6. Cell adhesion

Cell adhesion in the scaffolds was evaluated by staining the actin filaments after 24 h of cell culture (Fig. 5). The images indicate that cells attached and spread on all scaffold surfaces. No differences in cell morphology or preferential orientation were observed between the scaffolds.

3.7. Scaffold cytocompatibility and proliferation

hMSCs were cultured in the presence of 24- and 48-h scaffold-conditioned media to assess their potential toxicity. According to ISO 10993-5, toxicity is considered when a minimum of 30 % cell death

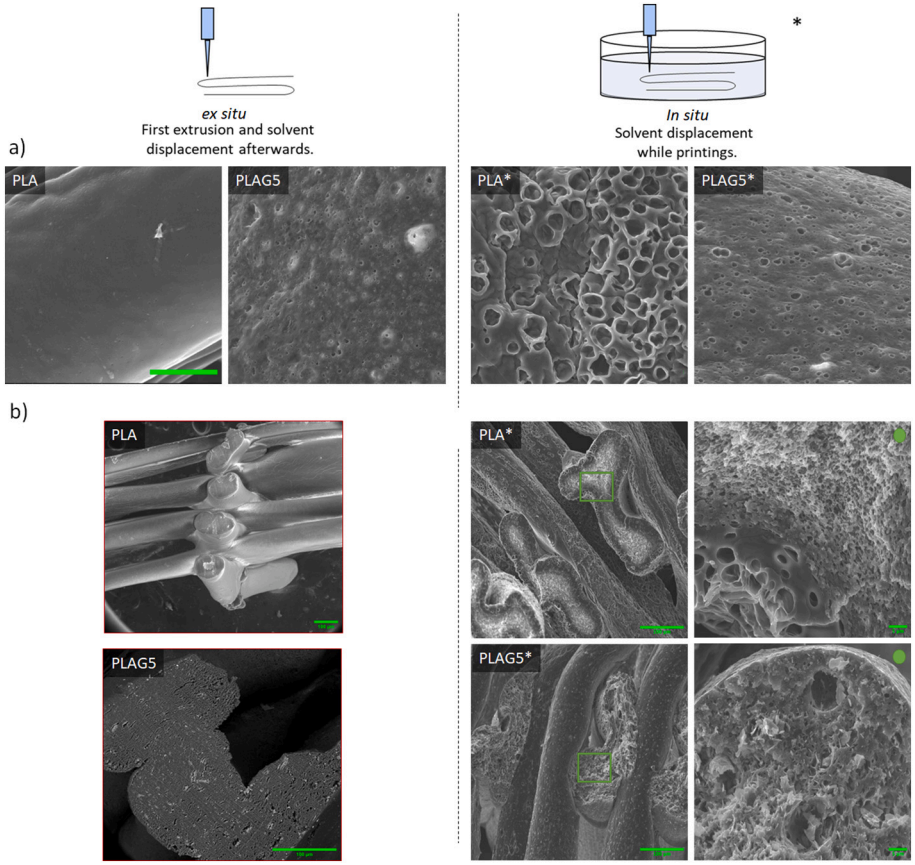

Fig. 2. Scaffold microporosity is dependent on the way the solvent is displaced at the moment of 3D printing. (a) Scaffold surface imaged by FE-SEM using different methods of solvent displacement (scale bar is 20 μm). (b) Scaffold cross-sections (scale bar is 20 μm).

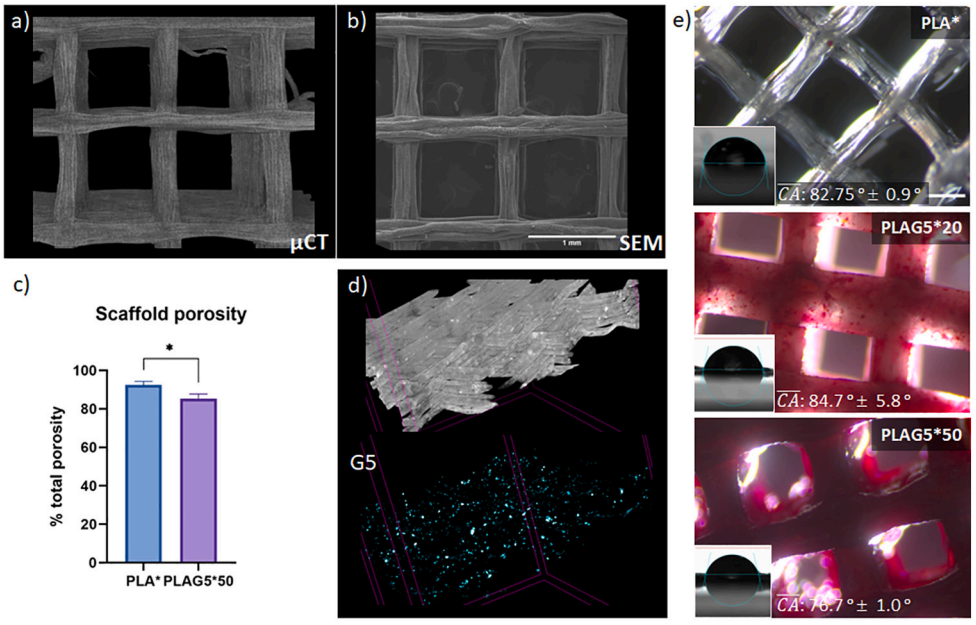

Fig. 3. Scaffold porosity and G5 incorporation. (a) μCT reconstruction of the scaffolds and (b) FE-SEM image to compare with μCT reconstruction (scale bar is 1 mm). (c) Quantification of scaffold porosity. (d) Representation of the G5 distribution (blue) by μCT. (e) Alizarin red staining and the respective contact angle of the different scaffolds. Increased staining intensity can be seen from the top (PLA*) to the bottom (PLAG5*50 %). CA is the median value for the contact angle. Data are expressed as the mean of three replicates. *p (0.01–0.05).

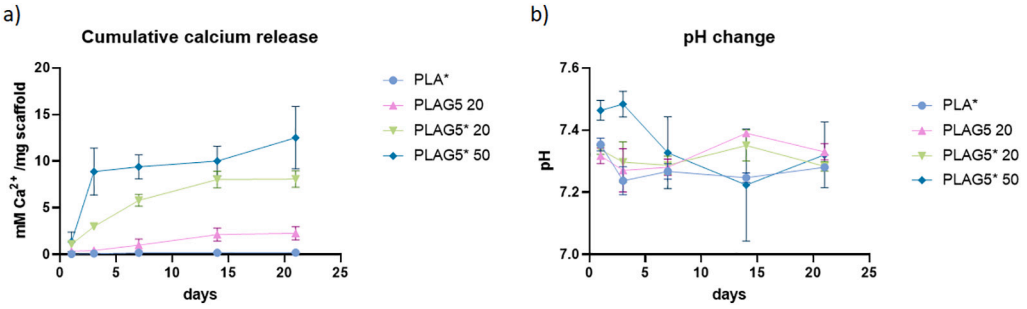

Fig. 4. Scaffold calcium release and pH variation. (a) Cumulative calcium release. (b) pH changes after 21 days in HEPES.

Table 3
Scaffold thermal and mechanical properties. Statistical differences with PLA* scaffolds are indicated with an asterisk (*), if any.

Material	T_g (°C)	Remaining G5 (%)	E modulus (MPa)
PLA*	60.36 ± 0.39	0 %	6.12 ± 1.47
PLAG5*20	59.49 ± 0.49	13.86 %	9.03 ± 2.48
PLAG5*50	60.27 ± 0.08	30.65 %	5.02 ± 0.35

occurs. Our scaffolds' maximum percentage of cell death was around 15 %; as a result, they were not considered toxic (Fig. 6A). The addition of conditioned media resulted in increased proliferation over time for all conditions tested; however, proliferation in the presence of scaffolds with conditioned media containing G5 at 50 % was found to be lower compared to PLAG5*20 and PLA* (Fig. 6B).

3.8. Alizarin red staining

Alizarin red staining was performed to assess the potential of hMSCs for tissue calcification after being stimulated with degradation products from the scaffolds. After five days in the presence of conditioned media, a positive alizarin red staining was observed in all conditions (Fig. 6C). Interestingly, higher mineralization levels could be observed when cells were stimulated with the conditioned media obtained from PLAG5*50 scaffolds.

3.9. VEGF release

hMSCs were cultured for five days in the presence of conditioned media to determine the amount of VEGF released (Fig. 7). An increase in VEGF levels may be observed on day 1 for PLAG5*50 scaffolds, reaching the highest levels of VEGF on day 3. PLAG5*20 scaffolds also showed an increase in VEGF levels after three days of culture. On day 5, no differences were observed among all conditions tested.

3.10. Biocompatibility and angiogenic response in vivo

A subcutaneous *in vivo* mouse assay was performed to assess the scaffold-tissue integration and the angiogenic response (Fig. 8A).

A semiquantitative histological assessment of the inflammation reaction was made (Fig. 8B). Results showed that all scaffolds induced a mild to moderate reaction, compatible with the process of scaffold implantation. Despite that, PLAG5*50 scaffolds tended to inflame less than the rest of the conditions.

Overall, all conditions showed blood vessel infiltration inside the scaffold area (Fig. 9). Samples were stained with CD31, a protein

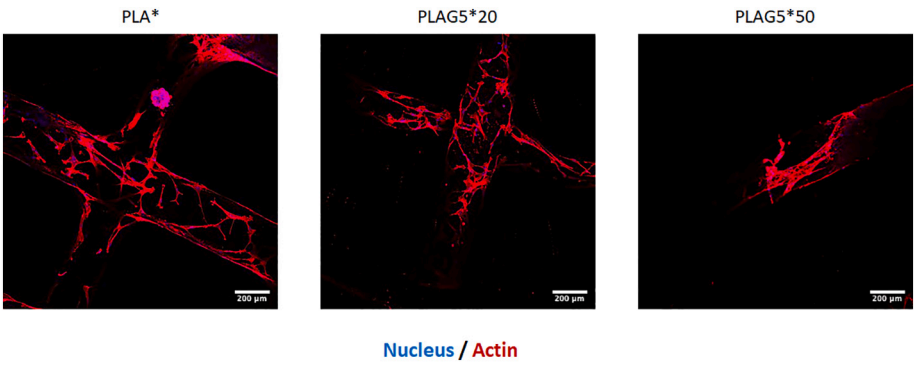

Fig. 5. Images showing hMSCs attached to scaffolds at 24 h post-seeding. Cells showed their characteristic spindle-like shape and were distributed throughout the scaffolds. Red: actin; Blue: nuclei (scale bar is 200 µm).

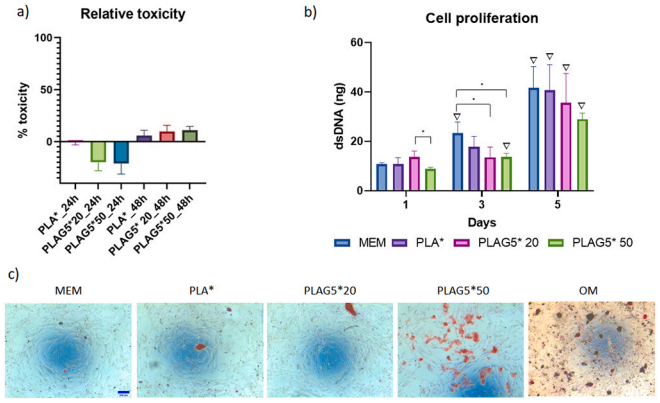

Fig. 6. Scaffold-induced toxicity, proliferation, and cell differentiation. hMSCs were cultured with scaffolds SN to assess cell behavior. (a) Percentage of toxicity after 24 and 48 h post-stimulation. (b) Cell proliferation after five days post-stimulation. (c) Representative images of alizarin red staining of the calcium deposits after five days of stimulation in standard media (Scale bar 200 µm). Positive control included is osteogenic media (OM).

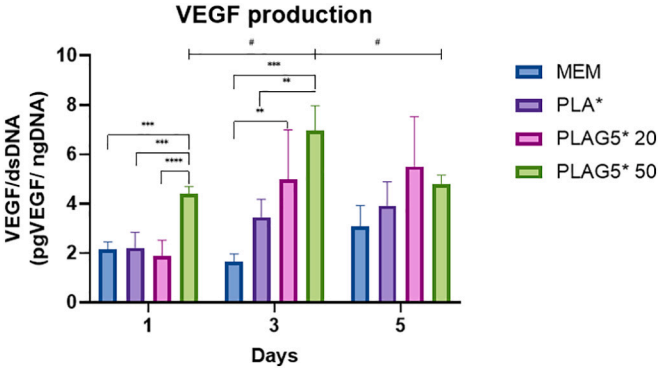

Fig. 7. VEGF production by hMSCs after scaffold SN stimulation. VEGF secretion by hMSCs at five days post-stimulation. Values were normalized by the total dsDNA (data are expressed as the mean of four replicates). **p (0.001–0.01), *** p (0.0001–0.001), **** $p < 0.0001$. For differences between time points, #p (0.01–0.05).

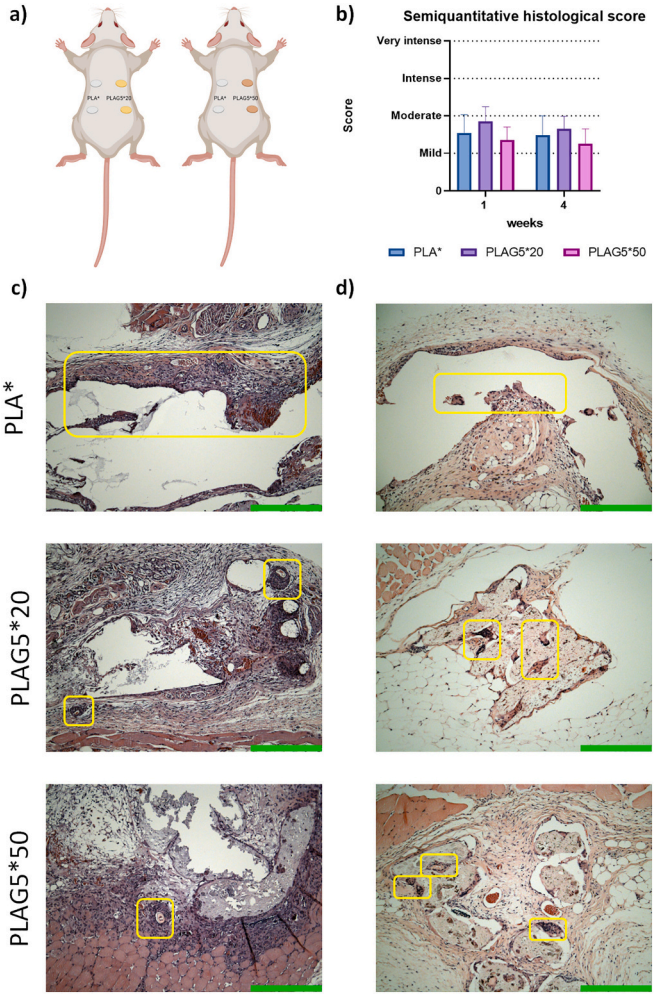

Fig. 8. Analysis of the biocompatibility on an *in vivo* subcutaneous model in mice. (a) Scheme showing the implantation procedure performed. (b). Semiquantitative histological scores for each of the scaffolds. (c) Representative images for week one and (d) week 4 showing H&E (scale bars are 313 µm). Marked in yellow are inflammatory infiltrates, as well as multinucleated giant cells.

expressed in the endothelial cell unions [40]. Results showed that all the conditions presented similar vessel numbers inside the scaffold area (Fig. 9A and C).

The samples were later stained against αSMA to detect vessel walls. αSMA was present in smooth muscle cells that surround endothelial cells and help to stabilize the vessel [41,42]. Vessel walls were thinner and incomplete after one week and became thicker and more stable after four weeks for all conditions studied (Fig. 9B-C).

The vessel thickness of PLAG5*20 scaffolds increased after one and four weeks compared to PLA* scaffolds. In addition, PLAG5*50 scaffolds increased vessel thickness after four weeks, showing the thicker vessels

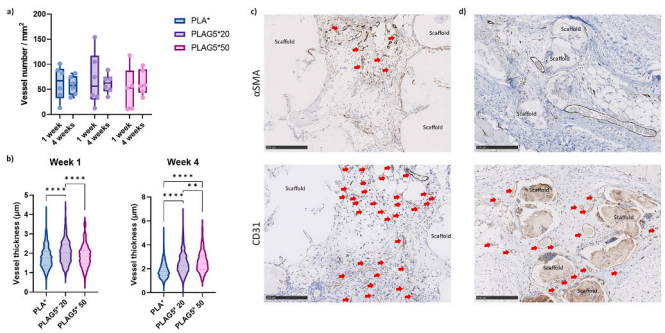

Fig. 9. Analysis of the angiogenic potential on an *in vivo* subcutaneous model in mice. (a) Quantification of CD31+ vessels inside the scaffold area. (b) Quantification of the wall vessel thickness one and four weeks post-implantation. (c) Representative images for week one) and (d) week four showing vessel maturation state. Top: αSMA+ vessel walls. Arrows indicate non-complete vessels. Bottom: CD31+ vessels. Arrows show vessels inside the scaffold area. These images correspond to the PLAG5*50 scaffolds but were results were equivalent for all conditions tested (scale bars are 250 μm). *p (0.01–0.05), **p (0.001–0.01), *** p (0.0001–0.001), **** $p < 0.0001$.

among all conditions tested (Fig. 9B).

4. Discussion

In this study, 3D printing, and solvent displacement approaches were combined to obtain a feasible layer-by-layer material deposition and to control the gross structure of the construct. PLA and G5 were used to manufacture these scaffolds. G5 are CaP-based submicrometric particles that had previously demonstrated angiogenic properties [31], as well as enhanced wound healing [32,33]. This combination was chosen to match the properties of bone. As G5 is brittle, PLA ensures the replication of bone mechanical properties, whereas G5 mimics the bone inorganic phase. The material, combined with the 3D printing process, permits the manufacture of a bone ECM-mimicking scaffold with high interconnected porosity to allow vessel infiltration.

Our results showed that our materials could be 3D printed with high shape fidelity. The scaffold's planar structure was highly reproducible with pore values near the theoretical design. In addition, PLA scaffolds had smaller pores compared to scaffolds containing G5. PLA is more flexible when G5 particles are not incorporated, so it may contract a bit once precipitated due to increased scaffold rigidity. Printability indexes corroborated that the scaffold pores were square as planned, with little deformation or contraction overall. Moreover, strut values showed similar values to the planned design. However, cross-sections revealed that the strut was not circular. Our final height would be close to the value calculated by multiplying the diameter of the scaffold strut by the number of layers. However, this was not the case with our final scaffolds (data not shown). FE-SEM images did not show any layer overlapping, and *ex-situ* displacement shows more rounded struts, which suggests that the *in situ* solvent displacement induced this strut deformation.

The choice of solvent and non-solvent had an impact on the final scaffold micro-nanostructure. Acetone/water was used as the solvent/non-solvent pair. Our results showed that the way the solvent is displaced affected the scaffold microstructure. A rapid and constant displacement (*in situ*) leads to a more porous surface. On the other hand, by displacing the acetone at the end (*ex situ*), its partial evaporation during the printing process results in shrinkage and compaction of the polymer chains and, therefore, in a smoother surface. The effect of the solvent/non-solvent interaction also affects the scaffold's inner microstructure. PLA scaffolds presented a homogeneous compacted strut, whereas PLA* resulted in a core-shell-like structure, which can be explained by the outer PLA's rapid precipitation and the water's slower diffusion rate inside the strut [43]. This effect was attenuated when G5 was incorporated, probably due to the increase in hydrophilicity caused by the particles, allowing the solvent to percolate more easily through the structure, resulting in a more homogeneous cross-section image. Despite this, some voids could be observed in the center of the strut rather than on the surface. These results followed the model proposed by Smolders, in which the kinetics of liquid-liquid de-mixing determined the formation of different microstructures on cellulose acetate films [44]. In the same manner, acetone-water de-mixing dynamics affected the microporosity on our scaffolds.

Following a previously published Eq. [45], the theoretical macroporosity for the scaffolds was calculated as 86.9 %. By analyzing microCT images, we confirmed that adding large amounts of G5 results in structural distortion (Table S1 in the supplementary material). Results showed that PLA* and PLAG5*50 scaffolds presented 92.5 and 85.3 % macroporosity, respectively. The increase in the macroporosity for the PLA* scaffold may come from the strut shrinkage, whereas G5 may counteract this effect. Other PLA constructs made with 3D printing also showed this high porosity percentage, which is superior to the theoretical values [46]. Indeed, the control of high levels of porosity is needed to allow the diffusion of nutrients and oxygen into the scaffold, which will enhance cell migration and survival [47–50]. As it was aforementioned, to achieve good necessary osteointegration, the overall scaffold porosity should be above *60–70%* [8,9,46]. Therefore, we can conclude that our scaffolds will allow this nutrient and oxygen diffusion, enabling the proper integration with the tissue.

Alizarin red staining confirmed the presence of the particles in our scaffolds, and as expected, the wettability of the PLA surface increased when G5 reached 50 % of loading. These results agree with previous reports, in which the use of bioglass particles increased the polymer hydrophilicity and water absorption [51,52].

Although scaffolds containing G5 released titanium, sodium, and phosphate [32], Aguirre et al. demonstrated that calcium ions are the major contributor to the angiogenic response [29,53]. With the instant displacement of the solvent with water, an increase in calcium release was achieved. This can be attributed to increased porosity, which makes particles inside the PLA strut more readily available for degradation. Moreover, calcium was released within the millimolar physiological range needed to stimulate cells [54].

The G5 content of the scaffolds was lower than the theoretical, with a maximum loading of 30.65 %. This phenomenon is attributed to the use of water in the polymer precipitation, which may remove some G5 from the matrix. To the best of our knowledge, there are no previous reports describing the effect of the fabrication process on the effective ceramic content.

In this work, PLA 70 %LL/30 %DL was chosen because of its low degree of crystallinity [25,26,38,55]. This means that scaffolds will degrade faster than other polymers such as polycaprolactone or crystalline L-PLA, which may take years to completely degrade [56]. To study whether PLA dissolution or the 3D printing process affected its crystallinity, the thermal properties using DSC were assessed. Results showed that the processability of the material did not affect its intrinsic T_g value, and therefore the polymer structure was intact. As expected, the addition of the particles neither affected the polymer structure, since blends were used nor were there further interactions between the polymer and the particles [57]. PLA was still amorphous at the end of the process as the rapid precipitation with water may prevent polymer chain rearrangement [39,58].

Scaffolds showed mechanical resistance in the range of MPa, and the addition of the particles did not affect the mechanical properties of the scaffolds. However, a maximum compressive modulus for the formulation containing 20 % of G5 can be observed. G5 could act as a reinforcement for the PLA, achieving good interaction due to the high surface area of the particles (due to their submicrometric size), as well as to their strong electrostatic interactions (PLA being negatively charged, and G5 positively charged) [8,59]. Despite this, increasing the number of G5 in the formulation raises the number of interfaces, increasing the probability of suffering cracks, which makes them less mechanically

stable [8]. In contrast, although this design was selected to favour the infiltration of cells, the scaffold's overall porosity can be modulated easily to fine-tune their overall mechanical properties [45,60], suggesting the possibility of achieving a scaffold upon mechanical requirements.

Our scaffolds supported hMSCs adhesion and spreading. These results are in line with previous studies reporting similar cell interactions with PLA surfaces [61]. Although PLA is on the limit of hydrophilicity, all our scaffolds presented micro- and nano-porosity, which increases both the surface area and a local tridimensional topography, promoting the interaction with proteins and cells. In addition, the preincubation time with culture media enhances serum protein adsorption, making it even easier for cells to attach to the structures [62].

Our results indicate that released by-products did not affect cell viability. Overall, the released products of these scaffolds were all biocompatible and easily metabolized by cells [61].

All scaffolds supported the proliferation of hMSCs, although the growth rate seems slower when increasing the concentration of particles in the scaffolds. Since a decrease in cell proliferation is a feature of cell differentiation [63], whether MSCs were changing into a more mature phenotype was analyzed. Cells exposed to PLAG5*50 scaffolds showed increased mineralization at the end of the culture period. These observations are in line with Quarles et al. who reported that MC3T3-E1 cells entering an intermediate differentiation stage showed decreased proliferation and increased ALP and mineralization deposition [63]. Notice that PLA* control also had a good proliferative behavior. Several studies reported it as a signaling molecule, which may affect several cellular processes, including proliferation [64,65].

Bone is a highly vascularized tissue, and the link between angiogenesis and bone healing has long been discussed in the bibliography [66–68]. For instance, several studies described the impairment of bone healing because of lack of or diminished angiogenesis [69,70]. Therefore, different strategies regarding bone tissue engineering have focused on promoting vascularization. Some involve the use of biological factors, such as cellular approaches using mesenchymal stem cells or angiogenic factors and small molecules [71]. Others use microsurgical procedures such as the Masquelet or the AV-Loop [6]. Bioglasses have also been an object of research in the angiogenesis for BTE strategies over the last years, although hardly ever considering calcium ions as a proangiogenic factor [72–78]. In this study, angiogenesis in a localized manner was stimulated using calcium/phosphate-based particles (G5) without the use of biological factors. Our results showed that scaffolds containing calcium-releasing particles promoted VEGF release from hMSCs, which has been shown to act as a secondary messenger to promote chemotaxis in endothelial progenitor cells [31]. Other studies have also reported an increase in VEGF among other factors *in vitro* upon bioglass stimulation [28,31,79–81]. Although some of these do not stress the effect of each ion, it was previously reported that calcium elicits the angiogenic response through the calcium-sensing receptor (CaSR) present in cells [28]. Several cations also had been reported to be angiogenic stimulators, such as cobalt and copper [72,82–85], but having control of the angiogenic response with one widely recognized metabolite may be an excellent option to minimize the use of other ions, small molecules, or growth factors whose side effects are unclear. Our scaffolds stimulated VEGF production on BM-hMSCs during the first three days, suggesting an early angiogenic response. Angiogenesis at the early stages is needed in bone healing to promote cell infiltration, oxygenation, and formation of the bony callus [86]. Therefore, triggering angiogenesis in those early stages may enhance the recovery of non-union fractures.

The angiogenic potential of the scaffolds on the CAM model was tested. As may be observed in the supplementary information, our results showed that this model is not appropriate for checking materials that have relevant tridimensionality. No differences could be observed between PLA* and PLA* + VEGF. However, the VEGF concentration showed angiogenic effects on the CAM. Other studies also showed the effect of similar particles on the CAM, when included in mild hydrogels [39]. Therefore, one may assume that the 3D structure also affects angiogenesis to some extent.

The biocompatibility response in a mouse subcutaneous model was also assessed. Results showed that no scaffolds showed signs of necrotic tissue at any time tested. After four weeks, the addition of glass suggested a reduced inflammatory response of the tissue surrounding the scaffold. These results may be explained by the presence of glass that enhances the wettability of the scaffold, making them gentler to apply than pure polymeric ones. Also, subtle changes in scaffold macroporosity, scaffold surface topography, and strut size may contribute to modifying the whole degradation of the scaffold, thus, modifying cell recruitment [87].

The scaffolds' angiogenic response tested well. Our histological results showed that all scaffolds supported blood vessel infiltration. This is important when considering the fabrication of scaffolds for bone regeneration. As noted before, current approaches to tackling bone regeneration do not allow sufficient blood vessel infiltration to maintain tissue survival and integration of the implant. In this study, better vascularization of the constructs within a week was achieved, possibly due to the high interconnected porosity of our scaffolds. This strategy supports blood vessel infiltration without the need for external biological agents, which are costly and present adverse effects such as carcinogenesis [78,88].

Moreover, only scaffolds containing G5 showed significantly more developed blood vessels after four weeks of implantation. These were featured by thicker walls, larger lumens, and better integration with the surrounding tissues compared to those within scaffolds without G5 or at earlier stages of development. This is an important result that suggests that the vasculogenic stimuli evoked by the PLAG5*50 scaffolds may result in complete and functional vasculature in the long term. This maturation is needed to avoid haemorrhaging and inflammation, as well as to satisfy the nutritional and functional tissue demand [89]. Previous studies also showed that glass scaffolds with a similar composition enhanced vessel maturation [39]. Proper vascularization within the implant will favour the conversion of the osteochondral tissue into bone [66], so bone regeneration will be more efficient. In addition, calcium phosphate-based glass scaffolds have demonstrated osteogenic potential *per se* [90–95]. The released by-products of calcium phosphate glass scaffolds are responsible for osteoblast homing and activating their proliferation and differentiation [96]. Therefore, adding calcium phosphate G5 particles into 3D PLA scaffolds would benefit bone regeneration by favouring not only vessel infiltration, together with a hosting 3D structure, but also vessel maturation and osteogenesis.

5. Conclusions

In this study, 3D composite scaffolds of PLA and calcium phosphate particles (G5) were produced. The combination of the described solvent displacement and 3D printing process allows control of the entire 3D structure, porosity, and surface topography in a reproducible manner. The composite scaffold showed good biocompatibility and secretion of VEGF from hMSCs *in vitro*, which led to further endothelial cell recruitment and angiogenesis. Because of its 2D image acquisition nature, validation of 3D scaffolds in the CAM model was highly restricted. Thus, new models for the validation are required. Subcutaneous implantation *in vivo* indicated good scaffold integration and blood vessel infiltration as early as one week after implantation. The presence of the glass particles promoted blood vessel maturation, whereas the engineered 3D-printed pores allowed cell infiltration, encouraging tissue-scaffold integration. Hence, only scaffolds containing G5 showed more matured vessels after 4 weeks of implantation than control. Taken together, the combination of 3D printing technology to place the porosity in the right way and dimension, and pro-angiogenic degradation products, like calcium ions from glass particles, opens a very encouraging strategy for bone tissue engineering, synergically

enhancing the resulting vascularization and, therefore, better healing than current approaches.

Associated supplementary information

The supplementary information associated with this manuscript describes the procedure for the chorioallantoic membrane assay (CAM), the ImageJ plugin macro's code for the quantification of the generated blood vessels, and the results.

CRediT authorship contribution statement

Celia Ximenes-Carballo: Writing – original draft, Visualization, Validation, Methodology, Investigation, Formal analysis, Conceptualization. **Sergi Rey-Viñolas:** Writing – review & editing, Visualization, Resources, Methodology, Investigation. **Barbara Blanco-Fernandez:** Writing – review & editing, Visualization, Resources, Methodology, Investigation. **Soledad Pérez-Amodio:** Writing – review & editing, Visualization, Supervision, Methodology. **Elisabeth Engel:** Writing – review & editing, Visualization, Supervision, Resources, Funding acquisition. **Oscar Castano:** Writing – review & editing, Visualization, Supervision, Resources, Methodology, Funding acquisition, Conceptualization.

Declaration of competing interest

The authors declare that they have no known competing financial interests or personal relationships that could have appeared to influence the work reported in this paper.

Data availability

Data are available upon reasonable request.

Acknowledgments

This work has been funded with the support of the European Regional Development Fund (FEDER), the Spanish Ministry of Science and Innovation (MICINN), and the State Research Agency (AEI) with the Projects (refs. RTI2018-096320-B-C21, and RTI2018-097038-B-C22), the European Commission-Euronanomed nAngioderm Project (ref. JTC2018-103) funded through the Spanish Ministry of Science and Innovation (ref. PCI2019-103648), the Pathfinder-EU project BIO-ACTION GA-101098972, the *Tecnologies Emergents* program of the General Directorate for Research–Generalitat de Catalunya (ref. 001-P-001646, cofunded by the FEDER Operational Program of Catalonia 2014–2020), and the Spanish network of cell therapy (TERCEL) for financial support. Finally, the researchers thank the Generalitat de Catalunya (2017-SGR-359) and the Severo Ochoa Programme of the Spanish Ministry of Science and Innovation (MICINN—Grant SEV-2014-0425, 2015-2019 and CEX2018-000789-S, 2019-2023). Authors also thank the IBEC's Core Facilities for their help, expertise and the excellent maintenance of the equipments, and the MicroFabSpace and Microscopy Characterization Facility, Unit 7 of ICTS "NANBIOSIS" at IBEC. Finally, Authors thank the Scientific and Technological Centers of the University of Barcelona (CCiTUB) for the facilities availability and help.

Appendix A. Supplementary data

Supplementary data to this article can be found online at https://doi.org/10.1016/j.bioadv.2024.213985.

References

[1] C.S. Bahney, R.L. Zondervan, P. Allison, A. Theologis, J.W. Ashley, J. Ahn, T. Miclau, R.S. Marcucio, K.D. Hankenson, Cellular biology of fracture healing, J. Orthop. Res. 37 (2019) 35–50, https://doi.org/10.1002/jor.24170.
[2] E. Roddy, M.R. DeBaun, A. Daoud-Gray, Y.P. Yang, M.J. Gardner, Treatment of critical-sized bone defects: clinical and tissue engineering perspectives, Eur. J. Orthop. Surg. Traumatol. (2018), https://doi.org/10.1007/s00590-017-2063-0.
[3] G. Turnbull, J. Clarke, F. Picard, P. Riches, L. Jia, F. Han, B. Li, W. Shu, 3D bioactive composite scaffolds for bone tissue engineering, Bioact. Mater. 3 (2018) 278–314, https://doi.org/10.1016/J.BIOACTMAT.2017.10.001.
[4] C.J. Damien, J.R. Parsons, Bone graft and bone graft substitutes: a review of current technology and applications, J. Appl. Biomater. 2 (1991) 187–208, https://doi.org/10.1002/jab.770020307.
[5] C. Delloye, O. Cornu, V. Druez, O. Barbier, Bone allografts: what they can offer and what they cannot, J. Bone Jt. Surg. - British Volume 89-B (2007) 574–580. doi: https://doi.org/10.1302/0301-620X.89B5.19039.
[6] L. Vidal, C. Kampleitner, M. Brennan, A. Hoornaert, P. Layrolle, Reconstruction of large skeletal defects: current clinical therapeutic strategies and future directions using 3D printing, Front. Bioeng. Biotechnol. 8 (2020), https://doi.org/10.3389/fbioe.2020.00061.
[7] A.R. Amini, C.T. Laurencin, S.P. Nukavarapu, Bone tissue engineering: recent advances and challenges, Crit. Rev. Biomed. Eng. (2012), https://doi.org/10.1615/CritRevBiomedEng.v40.i5.10.
[8] N. Sachot, E. Engel, O. Castaño, Hybrid organic-inorganic scaffolding biomaterials for regenerative therapies, Curr. Org. Chem. 18 (2014), https://doi.org/10.2174/1385272819666140806200355.
[9] J.W. Jang, K.E. Min, C. Kim, J. Shin, J. Lee, S. Yi, Review: Scaffold Characteristics, Fabrication Methods, and Biomaterials for the Bone Tissue Engineering, Int. J. Precis. Eng. Manuf. 24 (3) (2023) 511–529, https://doi.org/10.1007/S12541-022-00755-7, 24 (2023).
[10] J. Zeltinger, J.K. Sherwood, D.A. Graham, R. Müeller, L.G. Griffith, Effect of pore size and void fraction on cellular adhesion, proliferation, and matrix deposition, Tissue Eng. (2001), https://doi.org/10.1089/107632701753213183.
[11] M. Rasoulianboroujeni, N. Kiaie, F.S. Tabatabaei, A. Yadegari, F. Fahimipour, K. Khoshroo, L. Tayebi, Dual porosity protein-based scaffolds with enhanced cell infiltration and proliferation, Sci. Rep. (2018), https://doi.org/10.1038/s41598-018-33245-w.
[12] A. Colin, J.Y. Boire, A novel tool for rapid prototyping and development of simple 3D medical image processing applications on PCs, Comput. Methods Programs Biomed. (1997), https://doi.org/10.1016/S0169-2607(97)01807-5.
[13] Y. Song, K. Lin, S. He, C. Wang, S. Zhang, D. Li, J. Wang, T. Cao, L. Bi, G. Pei, Nano-biphasic calcium phosphate/polyvinyl alcohol composites with enhanced bioactivity for bone repair via low-temperature three-dimensional printing and loading with platelet-rich fibrin, Int. J. Nanomedicine 13 (2018) 505–523, https://doi.org/10.2147/IJN.S152105.
[14] B.H. Shamaz, A. Anitha, M. Vijayamohan, S. Kuttappan, S. Nair, M.B. Nair, Relevance of fiber integrated gelatin-nanohydroxyapatite composite scaffold for bone tissue regeneration, Nanotechnology (2015), https://doi.org/10.1088/0957-4484/26/40/405101.
[15] A. Salerno, M. Fernández-Gutiérrez, J. San Román Del Barrio, C. Domingo, Bio-safe fabrication of PLA scaffolds for bone tissue engineering by combining phase separation, porogen leaching and scCO2 drying, J. Supercrit. Fluids (2015), https://doi.org/10.1016/j.supflu.2014.10.029.
[16] J.C. Moses, S.K. Nandi, B.B. Mandal, Multifunctional cell instructive silk-bioactive glass composite reinforced scaffolds toward Osteoinductive, Proangiogenic, and Resorbable Bone Grafts, Adv. Healthc. Mater. 1701418 (2017) 1–17, https://doi.org/10.1002/adhm.201701418.
[17] W. Yang, F. Yang, Y. Wang, S.K. Both, J.A. Jansen, In vivo bone generation via the endochondral pathway on three-dimensional electrospun fibers, Acta Biomater. (2013), https://doi.org/10.1016/j.actbio.2012.10.003.
[18] N. Thadavirul, P. Pavasant, P. Supaphol, DEVELOPMENT OF POLYCAPROLACTONE POROUS SCAFFOLDS BY COMBINING SOLVENT CASTING, PARTICULATE LEACHING, AND POLYMER LEACHING TECHNIQUES FOR BONE TISSUE ENGINEERING, J. Biomed. Mater. Res. A (2013), https://doi.org/10.1002/jbma.35010.
[19] S. Bose, S. Vahabzadeh, A. Bandyopadhyay, Bone tissue engineering using 3D printing, Mater. Today 16 (2013) 496–504, https://doi.org/10.1016/J.MATTOD.2013.11.017.
[20] X. Yuan, W. Zhu, Z. Yang, N. He, F. Chen, X. Han, K. Zhou, Recent advances in 3D printing of smart scaffolds for bone tissue engineering and regeneration, Adv. Mater. (2024) 2403641, https://doi.org/10.1002/ADMA.202403641.
[21] F.H. Liu, Synthesis of bioceramic scaffolds for bone tissue engineering by rapid prototyping technique, J. Solgel. Sci. Technol. 64 (2012) 704–710, https://doi.org/10.1007/s10971-012-2905-5.
[22] W. Xu, A. Pranovich, P. Uppstu, X. Wang, D. Kronlund, J. Hemming, H. Öblom, N. Moritz, M. Preis, N. Sandler, S. Willför, C. Xu, Novel biorenewable composite of wood polysaccharide and polylactic acid for three dimensional printing, Carbohydr. Polym. 187 (2018) 51–58, https://doi.org/10.1016/j.carbpol.2018.01.069.
[23] A. Grémare, V. Guduric, R. Bareille, V. Heroguez, S. Latour, N. L'heureux, J. C. Fricain, S. Catros, D. le Nihouannen, Characterization of printed PLA scaffolds for bone tissue engineering, J. Biomed. Mater. Res. A 106 (2018) 887–894, https://doi.org/10.1002/jbm.a.36289.
[24] A. Kumar, S. Mandal, S. Barui, R. Vasireddi, U. Gbureck, M. Gelinsky, B. Basu, Low temperature additive manufacturing of three dimensional scaffolds for bone-tissue

engineering applications: processing related challenges and property assessment, Mater. Sci. Eng.: R: Rep. 103 (2016) 1–39, https://doi.org/10.1016/j.mser.2016.01.001.
[25] H. Oliveira, S. Catros, C. Boiziau, R. Siadous, J. Marti-Munoz, R. Bareille, S. Rey, O. Castano, J. Planell, J. Amédée, E. Engel, The proangiogenic potential of a novel calcium releasing biomaterial: impact on cell recruitment, Acta Biomater. 29 (2016), https://doi.org/10.1016/j.actbio.2015.10.003.
[26] H. Oliveira, S. Catros, O. Castano, S. Rey, R. Siadous, D. Clift, J. Marti-Munoz, M. Batista, R. Bareille, J. Planell, E. Engel, J. Amédée, The proangiogenic potential of a novel calcium releasing composite biomaterial: Orthotopic in vivo evaluation, Acta Biomater. 54 (2017), https://doi.org/10.1016/j.actbio.2017.02.039.
[27] A. González-Vázquez, J.A. Planell, E. Engel, Extracellular calcium and CaSR drive osteoinduction in mesenchymal stromal cells, Acta Biomater. 10 (2014) 2824–2833. doi:https://doi.org/https://doi.org/10.1016/j.actbio.2014.02.004.
[28] A. Aguirre, A. González, M. Navarro, O. Castaño, J.A. Planell, E. Engel, Control of microenvironmental cues with a smart biomaterial composite promotes endothelial progenitor cell angiogenesis, Eur. Cell. Mater. 24 (2012) 90–106.
[29] A. Aguirre, A. González, J.A. Planell, E. Engel, Extracellular calcium modulates in vitro bone marrow-derived Flk-1+ CD34+ progenitor cell chemotaxis and differentiation through a calcium-sensing receptor, Biochem. Biophys. Res. Commun. 393 (2010) 156–161, https://doi.org/10.1016/j.bbrc.2010.01.109.
[30] A. Aguirre, J.A. Planell, E. Engel, Dynamics of bone marrow-derived endothelial progenitor cell/mesenchymal stem cell interaction in co-culture and its implications in angiogenesis, Biochem. Biophys. Res. Commun. 400 (2010) 284–291. doi:https://doi.org/https://doi.org/10.1016/j.bbrc.2010.08.073.
[31] A. López-Canosa, S. Pérez-Amodio, E. Engel, O. Castaño, Microfluidic 3D platform to evaluate endothelial progenitor cell recruitment by bioactive materials, Acta Biomater. 151 (2022) 264–277, https://doi.org/10.1016/j.actbio.2022.08.019.
[32] C. Navarro-requena, S. Pérez-amodio, Wound healing-promoting effects stimulated by extracellular calcium and calcium-releasing nanoparticles on dermal fibroblasts, Nanotechnology (2018), https://doi.org/10.1088/1361-6528/aad01f.
[33] S. Perez-Amodio, N. Rubio, O.F. Vila, C. Navarro-Requena, O. Castaño, A. Sanchez-Ferrero, J. Marti-Munoz, M. Alsina-Giber, J. Blanco, E. Engel, Polymeric composite dressings containing calcium-releasing nanoparticles accelerate wound healing in diabetic mice, Adv. Wound Care (New Rochelle) 10 (2020) 1–3, https://doi.org/10.1089/wound.2020.1206.
[34] N. Sachot, O. Castaño, H. Oliveira, J. Martí-Muñoz, A. Roguska, J. Amedee, M. Lewandowska, J.A. Planell, E. Engel, A novel hybrid nanofibrous strategy to target progenitor cells for cost-effective in situ angiogenesis, J. Mater. Chem. B 4 (2016) 6967–6978, https://doi.org/10.1039/C6TB02162J.
[35] N. Soltan, L. Ning, F. Mohabatpour, P. Papagerakis, X. Chen, Printability and cell viability in bioprinting alginate Dialdehyde-gelatin scaffolds, ACS Biomater Sci. Eng. 5 (2019) 2976–2987, https://doi.org/10.1021/acsbiomaterials.9b00167.
[36] L.S. Parentoni, R.C.S. Pozeti, J.F. Figueiredo, E.C. de Faria, The determination of total calcium in urine: a comparison between the atomic absorption and the ortho-cresolphtalein complexone methods, J. Bras. Patol. Med. Lab. (2001), https://doi.org/10.1590/s1676-24442001000400003.
[37] E.M. Gindler, J.D. King, Rapid colorimetric determination of calcium in biologic fluids with methylthymol blue, Am. J. Clin. Pathol. (1972), https://doi.org/10.1093/ajcp/58.5.376.
[38] T. Serra, M. Ortiz-Hernandez, E. Engel, J.A. Planell, M. Navarro, Relevance of PEG in PLA-based blends for tissue engineering 3D-printed scaffolds, Mater. Sci. Eng. C 38 (2014) 55–62, https://doi.org/10.1016/j.msec.2014.01.003.
[39] C. Navarro-Requena, J.D. Weaver, A.Y. Clark, D.A. Clift, S. Pérez-Amodio, Ó. Castaño, D.W. Zhou, A.J. García, E. Engel, PEG hydrogel containing calcium-releasing particles and mesenchymal stromal cells promote vessel maturation, Acta Biomater. (2017), https://doi.org/10.1016/j.actbio.2017.12.009.
[40] W.A. Muller, Getting leukocytes to the site of inflammation, Vet. Pathol. 50 (2013) 7–22, https://doi.org/10.1177/0300985812469883.
[41] L.A. Oosterhoff, H.S. Kruitwagen, M.E. van Wolferen, B.W.M. van Balkom, M. Mokry, N. Lansu, N.A.M. van den Dungen, L.C. Penning, T.C.F. Spanjersberg, J. W. de Graaf, T. Veenendaal, F. Zomerdijk, J.O. Fledderus, B. Spee, F.G. van Steenbeek, Characterization of endothelial and smooth muscle cells from different canine vessels, Front. Physiol. (2019), https://doi.org/10.3389/fphys.2019.00101.
[42] M. Wanjare, S. Kusuma, S. Gerecht, Perivascular cells in blood vessel regeneration, Biotechnol. J. (2013), https://doi.org/10.1002/biot.201200199.
[43] T. Phaechamud, S. Chitrattha, Pore formation mechanism of porous poly(dl-lactic acid) matrix membrane, Mater. Sci. Eng. C 61 (2016) 744–752, https://doi.org/10.1016/j.msec.2016.01.014.
[44] C.A. Smolders, A.J. Reuvers, R.M. Boom, I.M. Wienk, Microstructures in phase-inversion membranes. Part 1. Formation of macrovoids, J. Memb. Sci. 73 (1992) 259–275, https://doi.org/10.1016/0376-7388(92)80134-6.
[45] T. Serra, J.A. Planell, M. Navarro, High-resolution PLA-based composite scaffolds via 3-D printing technology, Acta Biomater. 9 (2013) 5521–5530, https://doi.org/10.1016/j.actbio.2012.10.041.
[46] M. Alizadeh-Osgouei, Y. Li, A. Vahid, A. Ataee, C. Wen, High strength porous PLA gyroid scaffolds manufactured via fused deposition modeling for tissue-engineering applications, Smart Mater. Med. 2 (2021) 15–25, https://doi.org/10.1016/j.smaim.2020.10.003.
[47] N. Annabi, J.W. Nichol, X. Zhong, C. Ji, S. Koshy, A. Khademhosseini, F. Dehghani, Controlling the porosity and microarchitecture of hydrogels for tissue engineering, Tissue Eng. Part B Rev. 16 (2010) 371–383, https://doi.org/10.1089/ten.teb.2009.0639.
[48] R. Wu, Y. Li, M. Shen, X. Yang, L. Zhang, X. Ke, G. Yang, C. Gao, Z. Gou, S. Xu, Bone tissue regeneration: the role of finely tuned pore architecture of bioactive scaffolds before clinical translation, Bioact. Mater. 6 (2021) 1242, https://doi.org/10.1016/J.BIOACTMAT.2020.11.003.
[49] F. Lu, R. Wu, M. Shen, L. Xie, M. Liu, Y. Li, S. Xu, L. Wan, X. Yang, C. Gao, Z. Gou, Rational design of bioceramic scaffolds with tuning pore geometry by stereolithography: microstructure evaluation and mechanical evolution, J. Eur. Ceram. Soc. 41 (2021) 1672–1682, https://doi.org/10.1016/J.JEURCERAMSOC.2020.10.002.
[50] F. Mukasheva, M. Moazzam, B. Yernaimanova, A. Shehzad, A. Zhanbassynova, D. Berillo, D. Akilbekova, Design and characterization of 3D printed pore gradient hydrogel scaffold for bone tissue engineering, Bioprinting 39 (2024) e00341, https://doi.org/10.1016/J.BPRINT.2024.E00341.
[51] N. Sachot, M.A. Mateos-Timoneda, J.A. Planell, A.H. Velders, M. Lewandowska, E. Engel, O. Castaño, Towards 4th generation biomaterials: a covalent hybrid polymer–ormoglass architecture, Nanoscale 7 (2015) 15349–15361, https://doi.org/10.1039/C5NR04275E.
[52] V. Maquet, A.R. Boccaccini, L. Pravata, I. Notingher, R. Jérôme, Preparation, characterization, and in vitro degradation of bioresorbable and bioactive composites based on bioglass®-filled polylactide foams, J. Biomed. Mater. Res. A 66 (2003) 335–346, https://doi.org/10.1002/jbm.a.10587.
[53] O. Castaño, N. Sachot, E. Xuriguera, E. Engel, J.A. Planell, J.H. Park, G.Z. Jin, T. H. Kim, J.H. Kim, H.W. Kim, Angiogenesis in bone regeneration: tailored calcium release in hybrid fibrous scaffolds, ACS Appl. Mater. Interfaces (2014), https://doi.org/10.1021/am500885v.
[54] E.M. Brown, R.J. MacLeod, Extracellular calcium sensing and extracellular calcium signaling, Physiol. Rev. 81 (2001) 239–297, https://doi.org/10.1152/physrev.2001.81.1.239.
[55] N. Sachot, A. Roguska, J.A. Planell, M. Lewandowska, E. Engel, O. Castaño, Fast-degrading PLA/ORMOGLASS fibrous composite scaffold leads to a calcium-rich angiogenic environment, Int. J. Nanomedicine 12 (2017) 4901–4919, https://doi.org/10.2147/IJN.S135806.
[56] V. Campana, G. Milano, E. Pagano, M. Barba, C. Cicione, G. Salonna, W. Lattanzi, G. Logroscino, Bone substitutes in orthopaedic surgery: from basic science to clinical practice, J. Mater. Sci. Mater. Med. 25 (2014) 2445–2461, https://doi.org/10.1007/s10856-014-5240-2.
[57] T. Ogoshi, Y. Chujo, Organic-inorganic polymer hybrids prepared by the sol-gel method, compos, Interfaces 11 (2005) 539–566, https://doi.org/10.1163/1568554053148735.
[58] J. Marti-Muñoz, E. Xuriguera, J.W. Layton, J.A. Planell, S.E. Rankin, E. Engel, O. Castaño, Feasible and pure P2O5-CaO nanoglasses: an in-depth NMR study of synthesis for the modulation of the bioactive ion release, Acta Biomater. (2019), https://doi.org/10.1016/j.actbio.2019.05.065.
[59] Z. Álvarez, O. Castaño, A.A. Castells, M.A. Mateos-Timoneda, J.A. Planell, E. Engel, S. Alcántara, Neurogenesis and vascularization of the damaged brain using a lactate-releasing biomimetic scaffold, Biomaterials (2014), https://doi.org/10.1016/j.biomaterials.2014.02.051.
[60] A. Boccaccio, A.E. Uva, M. Fiorentino, G. Mori, G. Monno, Geometry design optimization of functionally graded scaffolds for bone tissue engineering: a mechanobiological approach, PloS One 11 (2016), https://doi.org/10.1371/journal.pone.0146935.
[61] F. Diomede, A. Gugliandolo, P. Cardelli, I. Merciaro, V. Ettorre, T. Traini, R. Bedini, D. Scionti, A. Bramanti, A. Nanci, S. Caputi, A. Fontana, E. Mazzon, O. Trubiani, Three-dimensional printed PLA scaffold and human gingival stem cell-derived extracellular vesicles: a new tool for bone defect repair, Stem Cell Res. Ther. 9 (2018) 104, https://doi.org/10.1186/s13287-018-0850-0.
[62] R.A. Gittens, L. Scheideler, F. Rupp, S.L. Hyzy, J. Geis-Gerstorfer, Z. Schwartz, B. D. Boyan, A review on the wettability of dental implant surfaces II: biological and clinical aspects, Acta Biomater. 10 (2014) 2907–2918, https://doi.org/10.1016/j.actbio.2014.03.032.
[63] L.D. Quarles, D.A. Yohay, L.W. Lever, R. Caton, R.J. Wenstrup, Distinct proliferative and differentiated stages of murine MC3T3-E1 cells in culture: an in vitro model of osteoblast development, J. Bone Miner. Res. (1992), https://doi.org/10.1002/jbmr.5650070613.
[64] Y. Fang, Z. Li, L. Yang, W. Li, Y. Wang, Z. Kong, J. Miao, Y. Chen, Y. Bian, L. Zeng, Emerging roles of lactate in acute and chronic inflammation, Cell Commun. Signal. 22 (1) (2024) 1–22, https://doi.org/10.1186/S12964-024-01624-8, 22 (2024).
[65] Q. Yang, Long Zhang, J. Chen, L. Zhang, Lactate: a critical regulator of cell proliferation via anaphase promoting complex remodeling, MedComm. – Oncology 2 (2023) e38, https://doi.org/10.1002/MOG2.38.
[66] J. Kanczler, R. Oreffo, Osteogenesis and angiogenesis: the potential for engineering bone, Eur. Cell. Mater. 15 (2008) 100–114, https://doi.org/10.22203/eCM.v015a08.
[67] U. Saran, S. Gemini Piperni, S. Chatterjee, Role of angiogenesis in bone repair, Arch. Biochem. Biophys. 561 (2014) 109–117, https://doi.org/10.1016/j.abb.2014.07.006.
[68] A.P. Kusumbe, S.K. Ramasamy, R.H. Adams, Coupling of angiogenesis and osteogenesis by a specific vessel subtype in bone, Nature 507 (2014) 323–328, https://doi.org/10.1038/nature13145.
[69] M.R. Hausman, M.B. Schaffler, R.J. Majeska, Prevention of fracture healing in rats by an inhibitor of angiogenesis, Bone (2001), https://doi.org/10.1016/S8756-3282(01)00608-1.
[70] C. Lu, E. Hansen, A. Sapozhnikova, D. Hu, T. Miclau, R.S. Marcucio, Effect of age on vascularization during fracture repair, J. Orthop. Res. (2008), https://doi.org/10.1002/jor.20667.
[71] G. Nazirkar, S. Singh, V. Dole, A. Nikam, Effortless effort in bone regeneration: a review, J. Int. Oral Health 6 (3) (2014) 120–124.

[72] S. Chen, M. Michálek, D. Galusková, M. Michálková, P. Švančárek, A. Talimian, H. Kaňková, J. Kraxner, K. Zheng, L. Liverani, D. Galusek, A.R. Boccaccini, Multi-targeted B and co co-doped 45S5 bioactive glass with angiogenic potential for bone regeneration, Mater. Sci. Eng.: C (2020) 110909, https://doi.org/10.1016/j.msec.2020.110909.
[73] M. Navarro, S. del Valle, S. Martínez, S. Zeppetelli, L. Ambrosio, J.A. Planell, M. P. Ginebra, New macroporous calcium phosphate glass ceramic for guided bone regeneration, Biomaterials 25 (2004) 4233–4241, https://doi.org/10.1016/j.biomaterials.2003.11.012.
[74] M.A. Saghiri, A. Asatourian, J. Orangi, C.M. Sorenson, N. Sheibani, Functional role of inorganic trace elements in angiogenesis-part I: N, Fe, se, P, au, and ca, Crit. Rev. Oncol. Hematol. 96 (2015) 129–142, https://doi.org/10.1016/j.critrevonc.2015.05.010.
[75] M.A. Saghiri, A. Asatourian, J. Orangi, C.M. Sorenson, N. Sheibani, Functional role of inorganic trace elements in angiogenesis-part II: Cr, Si, Zn, cu, and S, Crit. Rev. Oncol. Hematol. 96 (2015) 143–155, https://doi.org/10.1016/j.critrevonc.2015.05.011.
[76] J. Li, D. Zhai, F. Lv, Q. Yu, H. Ma, J. Yin, Z. Yi, M. Liu, J. Chang, C. Wu, Preparation of copper-containing bioactive glass/eggshell membrane nanocomposites for improving angiogenesis, antibacterial activity and wound healing, Acta Biomater. 36 (2016), https://doi.org/10.1016/j.actbio.2016.03.011.
[77] O.F. Vila, J.R. Bagó, M. Navarro, M. Alieva, E. Aguilar, E. Engel, J. Planell, N. Rubio, J. Blanco, Calcium phosphate glass improves angiogenesis capacity of poly(lactic acid) scaffolds and stimulates differentiation of adipose tissue-derived mesenchymal stromal cells to the endothelial lineage, J. Biomed. Mater. Res. A 101 (A) (2013) 932–941, https://doi.org/10.1002/jbm.a.34391.
[78] A. Malhotra, P. Habibovic, Calcium phosphates and angiogenesis: implications and advances for bone regeneration, Trends Biotechnol. 34 (2016) 983–992, https://doi.org/10.1016/j.tibtech.2016.07.005.
[79] R.M. Day, Bioactive glass stimulates the secretion of Angiogenic growth factors and angiogenesis in vitro, Tissue Eng. 11 (2005).
[80] A. Leu, J.K. Leach, Proangiogenic potential of a collagen/bioactive glass substrate, Pharm. Res. 25 (2008) 1222–1229, https://doi.org/10.1007/s11095-007-9508-9.
[81] H. Keshaw, A. Forbes, R.M. Day, Release of angiogenic growth factors from cells encapsulated in alginate beads with bioactive glass, Biomaterials 26 (2005) 4171–4179, https://doi.org/10.1016/j.biomaterials.2004.10.021.
[82] V.T. Nguyen, B. Canciani, F. Cirillo, L. Anastasia, G.M. Peretti, L. Mangiavini, Effect of chemically induced hypoxia on osteogenic and Angiogenic differentiation of bone marrow mesenchymal stem cells and human umbilical vein endothelial cells in direct Coculture, Cells 9 (2020) 757, https://doi.org/10.3390/cells9030757.
[83] Y.C. Chai, L.F. Mendes, N. van Gastel, G. Carmeliet, F.P. Luyten, Fine-tuning pro-angiogenic effects of cobalt for simultaneous enhancement of vascular endothelial growth factor secretion and implant neovascularization, Acta Biomater. 72 (2018) 447–460, https://doi.org/10.1016/j.actbio.2018.03.048.
[84] G. Giavaresi, P. Torricelli, P.M. Fornasari, R. Giardino, R. Barbucci, G. Leone, Blood vessel formation after soft-tissue implantation of hyaluronan-based hydrogel supplemented with copper ions, Biomaterials 26 (2005) 3001–3008, https://doi.org/10.1016/j.biomaterials.2004.08.027.
[85] C. Wu, Y. Zhou, M. Xu, P. Han, L. Chen, J. Chang, Y. Xiao, Copper-containing mesoporous bioactive glass scaffolds with multifunctional properties of angiogenesis capacity, osteostimulation and antibacterial activity, Biomaterials 34 (2013) 422–433, https://doi.org/10.1016/j.biomaterials.2012.09.066.
[86] H. Schell, G.N. Duda, A. Peters, S. Tsitsilonis, K.A. Johnson, K. Schmidt-Bleek, The haematoma and its role in bone healing, J. Exp. Orthop. 4 (2017) 5, https://doi.org/10.1186/s40634-017-0079-3.
[87] E. Saito, Y. Liu, F. Migneco, S.J. Hollister, Strut size and surface area effects on long-term in vivo degradation in computer designed poly(l-lactic acid) three-dimensional porous scaffolds, Acta Biomater. (2012), https://doi.org/10.1016/j.actbio.2012.03.028.
[88] Y. Kuroda, T. Kawai, K. Goto, S. Matsuda, Clinical application of injectable growth factor for bone regeneration: a systematic review, Inflamm. Regen. 39 (2019) 1–10, https://doi.org/10.1186/s41232-019-0109-x.
[89] H. Gerhardt, C. Betsholtz, Endothelial-pericyte interactions in angiogenesis, Cell Tissue Res. 314 (2003) 15–23, https://doi.org/10.1007/s00441-003-0745-x.
[90] J.A. Inzana, D. Olvera, S.M. Fuller, J.P. Kelly, O.A. Graeve, E.M. Schwarz, S. L. Kates, H.A. Awad, 3D printing of composite calcium phosphate and collagen scaffolds for bone regeneration, Biomaterials 35 (2014) 4026–4034, https://doi.org/10.1016/j.biomaterials.2014.01.064.
[91] Y. Chen, J. Wang, X.D. Zhu, Z.R. Tang, X. Yang, Y.F. Tan, Y.J. Fan, X.D. Zhang, Enhanced effect of β-tricalcium phosphate phase on neovascularization of porous calcium phosphate ceramics: in vitro and in vivo evidence, Acta Biomater. 11 (2015) 435–448, https://doi.org/10.1016/j.actbio.2014.09.028.
[92] I. Rajzer, E. Menaszek, R. Kwiatkowski, J.A. Planell, O. Castano, Electrospun gelatin/poly(ε-caprolactone) fibrous scaffold modified with calcium phosphate for bone tissue engineering, Mater. Sci. Eng. C 44 (2014) 183–190, https://doi.org/10.1016/j.msec.2014.08.017.
[93] E.S. Sanzana, M. Navarro, F. Macule, S. Suso, J.A. Planell, M.P. Ginebra, Of the in vivo behavior of calcium phosphate cements and glasses as bone substitutes, Acta Biomater. 4 (2008) 1924–1933, https://doi.org/10.1016/j.actbio.2008.04.023.
[94] X. Zhang, S. Meng, Y. Huang, M. Xu, Y. He, H. Lin, J. Han, Y. Chai, Y. Wei, X. Deng, Electrospun gelatin/β-TCP composite nanofibers enhance osteogenic differentiation of BMSCs and in vivo bone formation by activating Ca2+-sensing receptor signaling, Stem Cells Int. 2015 (2015), https://doi.org/10.1155/2015/507154.
[95] M.S. Fernández, J.I. Arias, M.J. Martínez, L. Saenz, A. Neira-Carrillo, M. Yazdani-Pedram, J.L. Arias, Evaluation of a multilayered chitosan-hydroxy-apatite porous composite enriched with fibronectin or an in vitro-generated bone-like extracellular matrix on proliferation and diferentiation of osteoblasts, J. Tissue Eng. Regen. Med. 6 (2012) 497–504, https://doi.org/10.1002/term.455.
[96] Y.C. Chai, A. Carlier, J. Bolander, S.J. Roberts, L. Geris, J. Schrooten, H. van Oosterwyck, F.P. Luyten, Current views on calcium phosphate osteogenicity and the translation into effective bone regeneration strategies, Acta Biomater. (2012), https://doi.org/10.1016/j.actbio.2012.07.002.